Optics Letters

Octupole electrode pattern for tuning forks vibrating at the first overtone mode in quartz-enhanced photoacoustic spectroscopy

Pietro Patimisco,[1,2] Angelo Sampaolo,[1] Marilena Giglio,[1] Verena Mackowiak,[3] Hubert Rossmadl,[3] Bruno Gross,[3] Alex Cable,[4] Frank K. Tittel,[2] and Vincenzo Spagnolo[1,2,*]

[1]PolySense Lab–Dipartimento Interateneo di Fisica, University and Politecnico of Bari, Via Amendola 173, Bari, Italy
[2]Department of Electrical and Computer Engineering, Rice University, 6100 Main Street, Houston, Texas 77005, USA
[3]Thorlabs GmbH, Hans-Boeckler-Straße 6, 85221 Dachau, Germany
[4]Thorlabs, Inc., 56 Sparta Ave., Newton, New Jersey 07860, USA
*Corresponding author: vincenzoluigi.spagnolo@poliba.it

Received 9 February 2018; accepted 17 March 2018; posted 21 March 2018 (Doc. ID 322940); published 11 April 2018

The design, realization, and performance analysis of an octupole electrode pattern configuration intended for the optimization of the charge collection efficiency in quartz tuning forks (QTFs) vibrating at the first overtone in-plane flexural mode is reported. Two QTFs having the same geometry, but differing in the electrode pattern deposited on the QTF prongs, have been realized in order to study the influence of the electrode pattern on the resonance quality factor and electrical resistance. A standard quadrupole pattern (optimized for the fundamental mode) and an octupole electrode layout have been implemented. Although both QTFs show the same resonance quality factor for the first overtone, the octupole pattern provides a reduction of the QTF electrical resistance by more than four times. The sensing performance of the two QTFs has been compared by employing them in a mid-IR quartz-enhanced photoacoustic sensor (QEPAS) system targeting a water absorption line. When operating at the first overtone mode, the QTF with an octupole electrode pattern provides a QEPAS signal more than two times higher with respect to the QTF employing the standard quadrupole configuration.

OCIS codes: (300.6340) Spectroscopy, infrared; (280.4788) Optical sensing and sensors; (110.5125) Photoacoustics.

https://doi.org/10.1364/OL.43.001854

Quartz-enhanced photoacoustic spectroscopy (QEPAS) is one of the most selective and sensitive trace-gas optical detection techniques, using quartz tuning forks (QTFs) to detect weak photoacoustic excitations and requiring extremely small sample volumes [1–4]. The implementation of custom QTFs in QEPAS gas sensing provides several advances, such as the extension of operation in the terahertz range [5–7] and the exploitation of single-resonator tube amplification systems, which are able to enhance the intensity of the acoustic waves deflecting the QTF prongs [8–10]. Custom QTFs designed to operate with fundamental flexural resonance mode frequency of a few kilohertz have initiated the implementation of the first overtone flexural modes for QEPAS sensing [11], resulting in the demonstration of two innovative approaches: (1) double-antinode excited QEPAS (DAE-QEPAS), in which a laser beam excites simultaneously the two resonance antinode vibrational points of a QTF operating with the first overtone flexural mode [12], providing a record signal-to noise amplification factor exploiting a dual acoustic micro-resonator system; and (2) dual-gas QEPAS detection, where two laser sources excite the antinodes of both the fundamental and the first overtone flexural modes, enabling the simultaneous detection of two gas species [13]. A single tube micro-resonator optimized for QTF overtone mode operation provided record QEPAS signal-to-noise gain factors of more than two orders of magnitude [8].

The fundamental and the first overtone modes exhibit a different quality factor because the associated loss mechanisms depend on the related vibrational dynamics and on the prongs geometry [14–17]. Hence, the QTF geometry can be designed to provide an enhancement of the overtone mode resonance Q-factors and a higher QEPAS signal-to-noise ratio with respect to the fundamental mode. However, in all QEPAS systems demonstrated so far, the electrodes layout of the employed QTFs employed a quadrupole pattern, matching the charge distribution generated by the in-plane fundamental mode vibration. Such electrode configuration partially impedes the excitation of the first overtone flexural mode since it should exhibit a different piezoelectric charge distribution.

In this Letter, we propose an innovative electrode pattern optimizing the first overtone flexural mode charge collection by analyzing the stress field distribution along the QTF prongs. The proposed electrode pattern has an octupole configuration, according to the change of the polarity along the prongs at the zero-stress point occurring for the first overtone vibrational mode. To provide a comparison between quadrupole and octupole electrode configurations in terms of QEPAS sensing

performance, both contact patterns have been deposited on two QTFs having the same geometry and size, which were implemented into a sensor system for water vapor trace detection.

When prongs of a tuning fork are in their natural oscillation motion, the stress produced along the prong can be expressed by a longitudinal tensor $\boldsymbol{\sigma}(x,y)$, where x and y identify a Cartesian plane orthogonal to the prong (aligned along the z axis). The stress induces a local polarization $\boldsymbol{p}(x,y)$ of quartz and charges appearing on the surface can be collected by electrical contacts appropriately deposited along the QTF prong. The polarization depends on the stress field as $\boldsymbol{p} = [\boldsymbol{d}]\boldsymbol{\sigma}$, where $[\boldsymbol{d}]$ is the quartz piezoelectric tensor. Assuming that the QTF axes correspond to the quartz crystal axes and considering the effects of the polarization perpendicular to the tensile stress, the relation between $\boldsymbol{p}$ and $\boldsymbol{\sigma}$ reduces to the scalar expression $p = -d_{11}\sigma$, where d_{11} is the longitudinal piezoelectric modulus. In the elastic regime, in which there is a linear relationship between the stress and the strain field, it can be shown that σ is proportional to the second derivative of the displacement for a bent prong. By using the formulation of the displacement derived by the Euler–Bernoulli equation, the tensile stress along the prong axis is given by [18]

$$\sigma(z) = A_n \left\{ \begin{array}{l} [-\cos(k_n z) - \cosh(k_n z)] + \left[\frac{\sin(k_n L)-\sinh(k_n L)}{\cos(k_n L)+\cosh(k_n L)}\right] \\ \times[-\sin(k_n z) - \sinh(k_n z)] \end{array} \right\}, \tag{1}$$

where the subscript n denotes different resonance mode numbers ($n = 0$ for the fundamental and $n = 1$ for the first overtone mode), A_n is the stress amplitude, and L is the prong length. k_n are constant values related to the resonance mode and, for the fundamental and the first overtone modes, $k_0 = 0.11\ \text{mm}^{-1}$ and $k_1 = 0.28\ \text{mm}^{-1}$, respectively. The curves in Fig. 1 show the distribution of the normalized strain along the prong as a function of the distance d from the prong-support junction for the fundamental and first overtone mode, obtained by using Eq. (1). The fundamental mode shows the highest stress antinode at $d = 0$. The first overtone mode shows two stress antinode points, one negative at $d = 0$ and one positive at $d = 9$ mm. For the fundamental vibrational mode, the sign of the strain distribution does not change over the entire length of the QTF prong whereas, for the first overtone mode, the strain direction changes along the length of the prong and, consequently, the sign of the piezoelectrically induced charges, which reverses at the zero-stress point. The electrode patterns deposited on QTF surfaces must be divided into separated zones corresponding to opposite generated electric field (and charges) areas in order to efficiently retrieve the piezoelectric signal provided by a specific flexural resonance mode.

The separation between electrodes of different polarity is located where the sign of the strain field reverses. For the fundamental flexural mode, the sign of the stress (and, thereby, of the generated charges) alternates between adjacent lateral prong surfaces, but remains the same along the prong length [see Fig. 2(a)]. Hence, a quadrupole electrode pattern should be employed. In addition, for the overtone mode, the sign of the stress is opposite over adjacent surfaces; nevertheless, the electrode pattern must be sectioned along the prong surface due to the presence of a zero-stress point, delimiting areas characterized by opposite stress signs and generated charges [see Fig. 2(b)]. This requires a dual-quadrupole electrode layout configuration, i.e., an octupole electrode pattern, for optimal charge collection. Based on this analysis, we designed and realized two QTFs having the same geometry and implementing a quadrupole (QTF-Q), as shown in Fig. 2(a), or an octupole (QTF-O) electrode pattern [see Fig. 2(b)]. The prong lengths were $L = 17$ mm, and their width $w = 1.0$ mm. By using the Euler–Bernoulli model, it is possible to determine the resonance frequencies of the fundamental and first overtone mode from the relation [18]

$$f_n = \frac{\pi t}{8\sqrt{12}L^2}\sqrt{\frac{E}{\rho}}\nu_n^2, \tag{2}$$

where $E = 0.72 \cdot 10^{11}\ \text{N/m}^2$ is the elastic Young modulus, and $\rho = 2650\ \text{Kg/m}^3$ is the density of the quartz. The first two solutions are $f_0 = 2913.4$ Hz ($\nu_0 = 1.194$) and $f_1 = 18245.5$ Hz ($\nu_1 = 2.998$). The selected prong geometry allows both resonance modes to be lower than 40 kHz and, therefore, suitable for QEPAS applications [11].

Both QTFs have been realized starting from a z-cut quartz wafer with a thickness $t = 0.25$ mm [19]. Different electrode layouts for the quadrupole configuration enhancing the

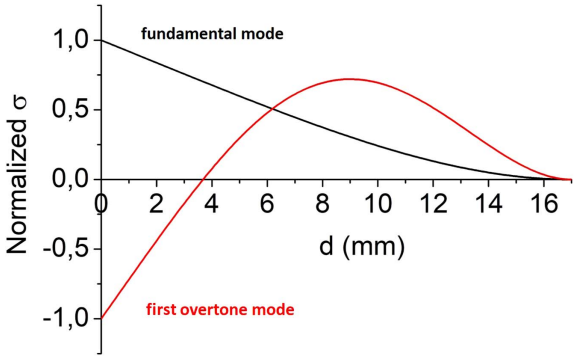

Fig. 1. One-dimensional normalized stress field distribution along the QTF prong as a function of the distance from the prong-support junction for the fundamental (black solid line) and the first overtone (red solid line) mode. The prong length is $L = 17$ mm.

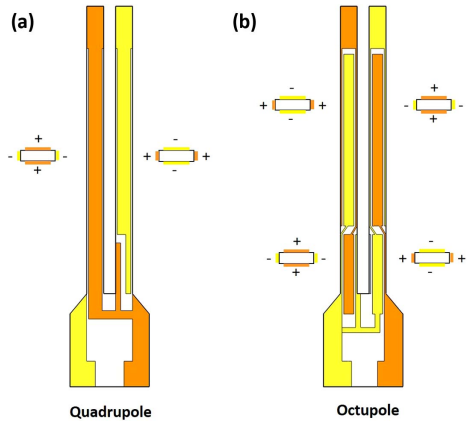

Fig. 2. (a) Schematic of the QTF-Q with a quadrupole electrode pattern. (b) Schematic of the QTF-O having an octupole electrode pattern. The pattern configuration is inverted in the QTFs' back surfaces. The small rectangles represent sections of the prong with the corresponding charge distributions.

fundamental mode have been proposed [20]. For the octupole configuration, a zero-stress point along the prong occurs at 3.8 mm from the prong-support junction (see Fig. 1). Hence, two quadrupole portions were considered for the electrode layout design of QTF-O, as shown in Fig. 2(b). The side electrode of a quadrupole portion is connected with the central electrode of the other portion by means of small electrode stripes. For both quadrupole and octupole configurations, the side electrode length is reduced on the top and wraps around at the end prongs in order to connect the two central (side) electrodes deposited on the opposite QTF-Q (QTF-O) surface.

The influence of the electrode layout on the main QTF characteristics, namely the resonance frequency, the quality factor, and the electrical resistance were investigated by using the experimental setup depicted in Fig. 3.

When the laser source is turned off, a waveform generator is used to provide a sinusoidal voltage excitation to the QTF, resulting in a piezoelectric charge displacement on its prongs via an inverse piezoelectric effect. The QTF current is converted to an output voltage by means of the trans-impedance preamplifier. The output voltage is sent to a lock-in amplifier to demodulate the signal at the same frequency of the waveform generator. The QTF-Q and QTF-O spectral responses at atmospheric pressure for the fundamental and the overtone modes are shown in Figs. 4(a) and 4(b), respectively.

The resonance curves of QTF vibrational modes have a Lorentzian lineshape. The resonance peak broadening is proportional to the energy losses occurring in the vibrating prongs. Furthermore, the larger the broadening, the higher are the losses. The quality factor Q is a fundamental parameter for characterizing the behavior of the QTF resonator subject to the influence of external perturbing forces. It is defined as the ratio of the energy stored in the resonator to the energy loss during each oscillation period and also can be calculated as the ratio between the resonance frequency and the full-width at half-maximum (FWHM) value of the resonance curve.

Each resonance curve was thereby fitted by using a pseudo-Lorentzian function [19,21] to determine the resonance, i.e., the peak, frequency, and its FWHM values, used to calculate the corresponding quality factor $Q = f/\text{FWHM}$. The obtained parameters are listed in Table 1. The small discrepancies between experimental and theoretical frequencies values are mainly due to (1) the gas damping effect, giving rise to an additional inertia for the vibrating prong, (2) the electrode gold pattern, altering the weight of each prong, and (3) the dependence of the elasticity modulus of quartz on the crystallographic axes orientation [19].

As previously mentioned, although the quadrupole electrode structure is designed to enhance the excitation of the fundamental mode of the QTF, it is also able to excite the first overtone mode whereas, in QTF-O, the fundamental mode is completely suppressed. The Q-factor for both QTFs vibrating at the overtone mode remains almost the same. This is to be expected because the quality factor is mainly affected by loss mechanisms occurring in the vibrating prongs (due to the interaction with the surrounding fluid and with the fixed support) and not by the charge collection efficiency [14,15].

The implementation of an octupole contact pattern strongly reduces (by a factor of ~4.4) the electrical resistance for the first overtone mode, demonstrating that this configuration collects the charges induced in the prongs more efficiently. Indeed, a large electrical conductance provides a high QEPAS signal, which implies that a QTF-O is expected to offer improved performances in terms of trace gas sensing when operated at the first overtone mode [10,18]. In order to verify this assumption, we implemented both QTFs in the QEPAS setup, depicted in Fig. 3. A single-mode continuous-wave quantum cascade laser (QCL) was employed as the excitation source to generate photoacoustic signals. The QCL targeted a water vapor absorption line falling at 1931.76 cm^{-1}, having a line strength of $3.2 \cdot 10^{-22}$ cm/molecule, according to a HITRAN database [22]. The laser beam was focused between the QTF prongs using a ZnSe lens with a focal length of 50 mm. An aluminum enclosure equipped with two mid-IR AR-coated windows was realized to accommodate and easily exchange the two QTFs.

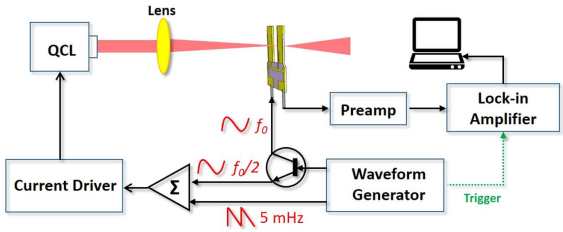

Fig. 3. Schematic diagram of the QEPAS experimental setup. The same setup was used to excite electrically the QTF by switching off the laser source and applying the sinusoidal excitation directly to the QTF. QCL, quantum cascade laser.

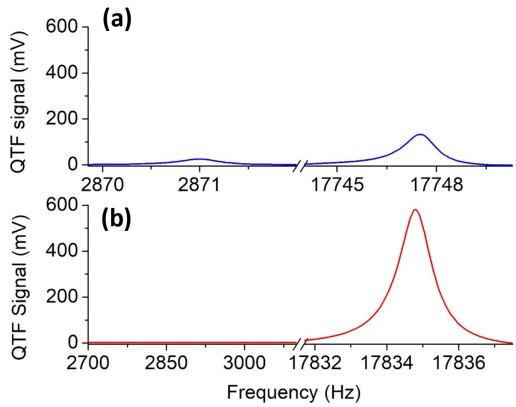

Fig. 4. Resonance curves measured at a fixed excitation level $V = 300$ mV and at atmospheric pressure for the (a) QTF-Q and (b) QTF-O.

Table 1. Resonance Frequency, Quality Factor, and Electrical Resistance Values Measured for the QTF-Q when Vibrating at the Fundamental or the First Overtone Mode and for the QTF-O when Vibrating at the First Overtone Mode

	QTF-Q	QTF-Q	QTF-O
	Fund. Mode	Overt. Mode	Overt. Mode
Frequency (Hz)	2870.99	17747.47	17834.79
Quality factor	5850	14500	15290
Resistance ($k\Omega$)	810.8	157.6	36.1

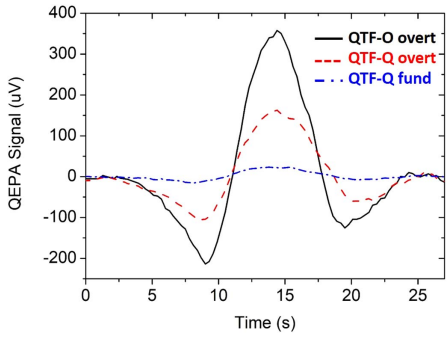

Fig. 5. QEPAS spectral scans of the water absorption line measured with the QTF-O operating at the first overtone mode (solid black curve) and the QTF-Q operating at the fundamental (dotted-dashed blue curve) or the overtone (dashed red curve) mode.

The housing was filled by standard air with a fixed 1.7% water vapor concentration at atmospheric pressure. The vertical position of the laser beam focus along the QTF axis was optimized in terms of a QEPAS signal. The laser was focused at 2 and 9.5 mm from the top of QTFs when vibrating at the fundamental or the first overtone mode, respectively [18]. The QEPAS sensor operates with a wavelength modulation and dual-frequency detection approach: the laser beam is wavelength-modulated at half of the selected resonance frequency (peak-to-peak amplitude of 250 mV), while the lock-in amplifier demodulates at the resonance frequency. The absorption line is acquired by applying a slow ramp (frequency of 5 mHz) to the current driver allowing a linear wavelength-scan. The QEPAS spectral scans of the selected water absorption line obtained for each vibrational mode of the investigated QTFs are shown in Fig. 5. The QEPAS spectra show that the peak value measured for QTF-O operating at the overtone mode is ~2.3 times higher than that obtained with a QTF-Q operating at the overtone mode and ~15.3 times higher when the QTF-Q is operated at the fundamental mode. This confirms that to fully exploit the photoacoustic performance of a QTF's first overtone mode, an octupole contact pattern configuration must be employed.

In conclusion, the obtained results demonstrate that employing an octupole electrode pattern configuration for a QTF vibrating at the first overtone mode is advantageous for two reasons. First, it lowers the electrical resistance with respect to the quadrupole electrode pattern, providing a reduction of the electrical power consumption when the QTF is employed as an electro-mechanical resonator in electronic devices, especially for battery-operated systems. Secondly, it provides higher signals when implemented in a QEPAS sensor system. Since the quality factor of the first overtone resonance mode is not affected by the employed contact pattern, this confirms that the QEPAS signal depends on the charge efficiency collection, i.e., is proportional to the electrical conductance. Finally, the octupole electrode layout can further enhance the performance of a DAE-QEPAS sensor, in which the two antinode points of the first overtone vibrational mode are simultaneously excited by the same laser beam [12].

Funding. Thorlabs GmbH (PolySense Lab); Welch Foundation (R4925U).

Acknowledgment. The authors from Dipartimento Interateneo di Fisica di Bari acknowledge financial support from THORLABS GmbH, within the joint research laboratory PolySense. Frank K. Tittel acknowledges support by the Welch Foundation.

REFERENCES

1. A. A. Kosterev, Y. A. Bakhirkin, R. F. Curl, and F. K. Tittel, Opt. Lett. **27**, 1902 (2002).
2. A. A. Kosterev, F. K. Tittel, D. Serebryakov, A. Malinovsky, and A. Morozov, Rev. Sci. Instrum. **76**, 043105 (2005).
3. P. Patimisco, G. Scamarcio, F. K. Tittel, and V. Spagnolo, Sensors **14**, 6165 (2014).
4. P. Patimisco, A. Sampaolo, L. Dong, F. K. Tittel, and V. Spagnolo, Appl. Phys. Rev. **5**, 011106 (2018).
5. V. Spagnolo, P. Patimisco, R. Pennetta, A. Sampaolo, G. Scamarcio, M. S. Vitiello, and F. K. Tittel, Opt. Express **23**, 7574 (2015).
6. A. Sampaolo, P. Patimisco, M. Giglio, M. S. Vitiello, H. E. Beere, D. A. Ritchie, G. Scamarcio, F. K. Tittel, and V. Spagnolo, Sensors **16**, 439 (2016).
7. Z. Li, C. Shi, and W. Ren, Opt. Lett. **41**, 4095 (2016).
8. H. Zheng, L. Dong, A. Sampaolo, H. Wu, P. Patimisco, X. Yin, W. Ma, L. Zhang, W. Yin, S. Jia, and F. K. Tittel, Opt. Lett. **41**, 978 (2016).
9. H. Zheng, L. Dong, A. Sampaolo, H. Wu, P. Patimisco, W. Ma, L. Zhang, W. Yin, L. Xiao, V. Spagnolo, S. Jia, and F. K. Tittel, Appl. Phys. Lett. **109**, 111103 (2016).
10. P. Patimisco, A. Sampaolo, H. Zheng, L. Dong, F. K. Tittel, and V. Spagnolo, Adv. Phys. X **2**, 169 (2016).
11. A. Sampaolo, P. Patimisco, L. Dong, A. Geras, G. Scamarcio, T. Starecki, F. K. Tittel, and V. Spagnolo, Appl. Phys. Lett. **107**, 231102 (2015).
12. H. Zheng, L. Dong, P. Patimisco, H. Wu, A. Sampaolo, X. Yin, S. Li, W. Ma, L. Zhang, W. Yin, L. Xiao, V. Spagnolo, S. Jia, and F. K. Tittel, Appl. Phys. Lett. **110**, 021110 (2017).
13. H. Wu, X. Yin, L. Dong, K. Pei, A. Sampaolo, P. Patimisco, H. Zheng, W. Ma, L. Zhang, W. Yin, L. Xiao, V. Spagnolo, S. Jia, and F. K. Tittel, Appl. Phys. Lett. **110**, 121104 (2017).
14. H. Hosaka, K. Itao, and S. Kuroda, Sens. Actuators A Phys. **49**, 87 (1995).
15. Z. Hao, A. Erbil, and F. Ayazi, Sens. Actuators A Phys. **109**, 156 (2003).
16. F. R. Blom, S. Bouwstra, M. Elwenspoek, and J. H. J. Fluitman, J. Vac. Sci. Technol. B **10**, 19 (1992).
17. K. Xu, IEEE Sens. J. **16**, 6184 (2016).
18. F. K. Tittel, A. Sampaolo, P. Patimisco, L. Dong, A. Geras, T. Starecki, and V. Spagnolo, Opt. Express **24**, A682 (2016).
19. P. Patimisco, A. Sampaolo, L. Dong, M. Giglio, G. Scamarcio, F. K. Tittel, and V. Spagnolo, Sens. Actuators B Chem. **227**, 539 (2016).
20. J. Ma, J. Xu, J. Duan, and H. Xu, Res. J. Appl. Sci. Eng. Technol. **5**, 1232 (2013).
21. D. I. Bradley, M. J. Fear, S. N. Fisher, A. M. Guénault, R. P. Haley, C. R. Lawson, G. R. Pickett, R. Schanen, V. Tsepelin, and L. A. Wheatland, Phys. Rev. B **89**, 214503 (2014).
22. http://www.hitran.org/.